ECPA
Budapest 2021

13th European Conference on Precision Agriculture

PRECISION AGRICULTURE '21

Edited by: **John V. Stafford**

Wageningen Academic
P u b l i s h e r s

Precision agriculture '21

edited by:
John V. Stafford

Papers presented at the 13th European Conference on Precision Agriculture
Budapest, Hungary
18-22 July 2021

Wageningen Academic
P u b l i s h e r s

Buy a print copy of this book at

www.WageningenAcademic.com/PA21

MINISTRY
OF AGRICULTURE

Preface

In this most unusual of years, the 13th European conference is being held – definitely online and, covid-19 depending, as a conventional conference in Budapest, Hungary. With so much uncertainty in the world, would prospective paper authors be too apprehensive to submit an abstract? Our fears were groundless, over 200 abstracts were submitted and assessed. As a result, 116 full papers were accepted for oral presentation.

That is a big relief as agriculture faces increasing challenges and precision agriculture plays a significant role in solving these challenges. So, as with previous conferences, this one is again timely and the papers published in these Proceedings form an important permanent record. PA research is increasing the world over and a good cross-section of results from that research is presented here. The Proceedings should form a useful reference source in the years to come.

The conferences have gained a good reputation because of the standard of the Proceedings. A strict approach has been taken to paper acceptance. Each draft paper has been assessed by two members of the Scientific Committee and by myself as Editor. Revised papers have been subjected to rigorous editorial processing so that the papers presented here approach the quality of papers in refereed journals. I would like to record my grateful appreciation to the members of the Scientific Committee who, amidst the busy schedule of research careers, have freely given their time and professional judgement to assess the conference papers. I would also like to thank Gabor Milics for persevering in organising the conference in the face of the pandemic and all the uncertainties that that has caused.

John V Stafford
Editor
Ampthill, UK.
john.stafford@silsoe-solutions.co.uk
April 2021

43. Distortion and mosaicking of close-up multi-spectral images

A. Krus[1], C. Valero[1*], J. Ramirez[1], C. Cruz[2], A. Barrientos[2] and J. del Cerro[2]

[1]*Universidad Politécnica de Madrid, ETSIAAB, Av. Puerta de Hierro 2, 28040 Madrid, Spain; constantino.valero@upm.es ●RCID 0003-4473-3209*

[2]*CAR (Consejo Superior de Investigaciones Científicas-Universidad Politécnica de Madrid), C. José Gutiérrez Abascal 2, 28006 Madrid, Spain*

Abstract

In precision agriculture (PA), vegetation indices (VI) are commonly used to evaluate the health of crops with the use of multi-spectral cameras. These are often mounted on drones and used at high altitudes, where the translation of focal points and subsequent changes in perspective do not pose any difficulties. In proximal sensing, however, these translations and distortions pose a significant challenge on data processing. In this work, a Parrot Sequoia camera was mounted at a fixed height of 1.2 m and used at 3 s and 1.5 s intervals on the field beneath. Reference imaging revealed that the multi-spectral lenses suffer from significant barrel distortion of 30%, while the higher resolution RGB lens has a barely distinguishable 1% pincushion distortion. The subsequent field images were stitched together using an open-source panorama software to automatically detect and correct distortions The resulting mosaics were then shifted to correct the relative position of the separate lenses, allowing for VI calculation with mm accuracy. This method allows for analysing single plants for inter-crop and even intra-crop variation.

Keywords: multi-spectral, lens distortion, image processing

Introduction

A commonly used indicator of crop health in precision agriculture (PA) are vegetation indices (VI). They are calculated using reflectance values obtained from a multi-spectral camera. These cameras often contain several lenses with physical filters. Usually, they are used at high altitudes, in the range of e.g. 60 m (Moriarty *et al.*, 2019) to 120 m (Fernández-Guisuraga *et al.*, 2018). In this set-up and at this scale, the inclination of the camera at the time of the picture, as well as the GNSS coordinates are essential for subsequent image stitching. Oftentimes an overlap of 60 to 80% is used between images (Franzini *et al.*, 2019; Moriarty *et al.*, 2019). Besides a variety of commercial software available for the mosaicking of these images, ever more complicated algorithms have been proposed, such as e.g. Jhan *et al.* (2018).

This work follows a more straightforward approach, such as e.g. Liang *et al.* (2019), adapted to a smaller scale terrestrial set-up and expanded to the near infra-red spectrum, where the current paper focusses on the image processing to allow for classic VI calculations, using only open-source software. This circumvents paying for commercial licensing while still ensuring satisfactory results, as well as reducing the previously mentioned complexity to a minimum for easier implementation. The objectives are two-fold, the first is to assess the amount of distortion present in the lenses of the multi-spectral camera used in an indoor set-up with open-source imaging software. The second is to use this information on close-range images of a crop row from the same sensor, and to obtain a distortion free seamless mosaic without the use of commercially licensed programs.

Materials and methods

Materials

The combination of sensors and (robotic) actuation stipulated in the SUREVEG project (Krus *et al.*, 2020) requires a mounting structure that ensures a constant distance from the soil and vegetation, mainly dictated by the reach of the selected robotic arm. The relevant parts of this structure are shown schematically in Figure 1a, where the position and orientation of the multi-spectral camera are indicated in red. The operational height is therefore constant at about 1.2 m for all measurements. The structure is propelled manually, at a speed that fluctuates between 0.2 and 0.3 m/s due to the roughness of the terrain. Images were recorded at a fixed time-interval of 3 s in 2019, which was halved in the 2020 measurements, corresponding to an advance of about 60-90 cm and 30-45 cm respectively. Note that the cart is mounted with other equipment as well, not included in this schematic, which may block part of the view depending on the equipment mounted at the time. This is discussed in more detail below.

The multi-spectral camera employed in this work was the Parrot Sequoia Camera (Parrot S.A., Paris, France), which captures both an RGB image and four spectral band images simultaneously. The distribution of these 5 lenses is shown in Figure 1b. The distances between the optical axes of the spectral cameras are 1.6-1.7 cm, with the exception of the RGB camera, which is centred between the spectral cameras with an offset of 1.3 cm. Three of the spectral bands have a bandwidth of 40 nm, around the following wavelengths: 550 nm for green (G), 660 nm for red (R), and 790 nm for near-infrared (NIR). Between the latter two, the red-edge (RE) band of only 10 nm is included around 735 nm. Each of the resulting images of 1.2 megapixel (MP) contains a horizontal and vertical field-of-view (HFOV × VFOV) of 62° and 49°, covering an area of about 144×109 cm when positioned at a 1.2 m height as shown above. The RGB camera on the other hand has a resolution of 16 MP, and a slightly larger FOV, resulting in a covered area of 150×112 cm when mounted at 1.2 m. Each measurement session is stored in a single zip folder, containing each of the subsequent photos in five-fold, where the RGB image is stored in jpg, whereas the spectral images are saved in tiff format. As stated in Jhan *et al.* (2017), the lens distortion of this camera is known to be significant. To detect the exact amount in percentages, two set-ups with wooden boards were photographed at heights of 95 and 120 cm respectively, one of which is shown in Figure 1c. The first consisted of flat narrow boards with coated edges, providing two straight lines per plank, as well as some metersticks to cross. The second consisted of only square wooden stakes with a spike at one end as used in outdoor trials, in two different orientations to maximize the referenced area within the photograph. As the latter was taken from the mobile structure, a part of the image was blocked by other cart mountings not relevant here, reducing the visible ground surface by 18%. In Figure 1c this blockage can be seen in the upper area. The lighting conditions indoors were sub-optimal in both set-ups but proved sufficient for the detection of the references.

The field used for the outdoor measurements is located at 40°26'38.9" N 3°44'19.3" W, Madrid, Spain. Each of the strips is planted with a single crop type at regular distances, and measures 1.40 m in width, to coincide with the mobile structure's wheelbase. At 10 running meters markers are present to guide the measurement length. This work focusses on the lines of cabbage of the 2019-2020 and 2020-2021 crop season.

Methods

Each zip file of the Sequoia camera is downloaded through its locally hosted WiFi connection. For the investigations of the lens distortions, a set of images from the indoor reference set-up is loaded into GNU Image Manipulation Program (GIMP), where the reference lines are selected manually and extracted, before being corrected for the lens distortion until achieving the straight-lined end result. Finally, the extracted areas before and after correction are coloured for clarity.

In the field trials, the stitching of the several images belonging to a single pass of the mobile structure was done semi-automatically in Hugin Panorama Editor. Matching features (or Control Points) are identified using Hugin's CPFind algorithm, and then manually checked for correctness. The area occluded by the structure's actuation is hereto excluded from the images, as this would result in perfect matches across the session since the area shows the mounted actuator from the same relative angle and distance throughout the measurement. The feature finding algorithm is applied to the RGB images and the green images separately, where the resulting points of the latter are then remapped onto the other spectral image sets, as their resolution is equal. The identified features are usually twigs or rocks in the soil, or casted shadows on sunny days. The green images were the most suitable of the spectral bands for this marking process. It should be noted that due to the small overlap (±20 cm) in the 2019 measurements, a large portion of the features was identified manually, whereas the shorter time-lapse used in 2020 allowed automatic identification. In each of the manually marked stitching lines, the number of identified features was set to a minimum of six to ensure proper distortion detection, where the markers should span the largest possible area. The results are stitched using the original photometric properties, i.e. without applying filters or corrections, as the irradiance sensor of the Sequoia is assumed to correct for changes in lighting conditions.

The alignment of each of the stitched spectral images was deduced through moving semi-transparent layers in GIMP, which can then be confirmed in e.g. Matlab or Python. Due to parallax, this shift depends largely on focal distance. Once the necessary translations of each channel were determined, the result was applied to each of the measurement sets allowing for vegetation index (VI) calculations at very high spatial resolution in each imaged crop row within the same program. The resolution obtained directly follows the resolution of the spectral lenses and the (close-range) mounting height.

Results

Reference set-ups

Both straight lined references, at 95 and 120 cm, revealed a necessary distortion correction of only 1% in the RGB images. This distortion is hardly visible as seen in the left images of Figures 2 and 3. The spectral images, however, required a correction of 30-33%, found to be consistent for all spectral bands. The difference of 3% between the two set-ups can be explained by the lines stemming from a wooden object that might not be perfectly clear, as well as the reduced contrast of the references in the lighting conditions used. As the amount of distortion is assessed manually, a difference of 3% is hardly visible, as can be expected when reviewing the impact of the 1% correction in the RGB images. This is, however, something that could be further looked into. As the stitching software automatically corrects these distortions, the exact amount does not have to be known for further processing.

Figure 1. (a) A schematic view of the relevant parts of the mounting structure, to which the camera is attached at a fixed height of 1.2 m from the soil, with its field-of-view indicated by the red cone. (b) The spatial distribution of the Parrot Sequoia lenses, with 4 spectral bands and a high resolution RGB camera at the bottom. (c) One of the two reference objectives used for quantifying the lens distortion, including partial blockage by other mounted structures.

Figure 2. The distortion found in the RGB image (left) and the spectral images (right) when taken at a height of 95 cm. Red: lines in the original image. Green: parallel lines, after correcting for a 1% pincushion and 30% barrel distortion, respectively.
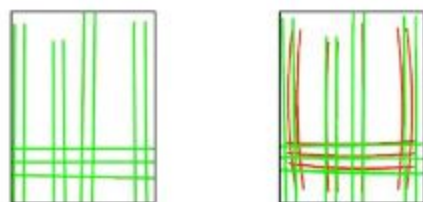

Figure 3. The distortion found in the RGB image (left) and the spectral images (right) when taken at a height of 120 cm. Red: lines in the original image. Green: parallel lines, obtained after correcting for a 1% pincushion and 33% barrel distortion, respectively.

Field images

In the field measurements, the sun cast rather sharp direct shadows, which on the one hand resulted in additional reference features at soil height, but on the other hand reduced the amount of information in the shadowy areas, affecting the distribution of VI values in the final images. The VI values on crop pixels are not affected, but the effect of shadows should be taken into account when accounting for larger areas for their evaluation, e.g. through averaging. The translation that ensures perfect alignment is listed in Table 1, yielding the correction as displayed in Figure 4. This correction was applied to all measurements of 2019 and 2020, as listed in Table 2. These shifts differ from those listed in Cardim Ferreira Lima *et al.* (2020) as a result of the different mounting height. Given the blocked area of the other mounting structure components, the area depicted in a spectral image is reduced from around 1.44 running m to about 1.10 m. The uneven surface and manual propulsion caused velocity fluctuations, which in the worst case resulted in images overlapping a mere 20 cm. This made the identification of sufficient features difficult at times, which means some measurements had to be repeated to ensure an overlap of at least six features. The low number of features provided little information on possible deformations to the stitching algorithm, which is why the overlap was doubled in the next year. Due to the manual positioning and moving speed, the number of images per row was 11-14 in 2019, and 30-40 in 2020. This variability can also be

Table 1. Fixed image translations with respect to the red (R) spectral band in pixels (x,y).

Image	Translation
Green (G)	(-27,0)
Near-infrared (NIR)	(-11,15)
Red-edge (RE)	(-23,17)

Figure 4. The 4 spectral images taken from slightly different perspectives, coloured here for clarity, both before (left) and after (right) translation correction.

Table 2. Field measurement dates and the setting of the camera used.

Date		Time-lapse setting, s
2019	26 September	3
	06 November	3
	12 November	3
	18 November	3
	27 November	3
2020	29 October	1.5
	06 November	1.5
	12 November	1.5

contributed to the extra distance before and after the 10 m markers that was recorded in varying amounts, resulting in some measurements spanning more than the 10 m of interest.

The 3 s image acquisition interval in 2019, proved to be labour intensive for image stitching. In Figure 5, a typical subsequent pair of images are reduced to their overlapping area, with some example
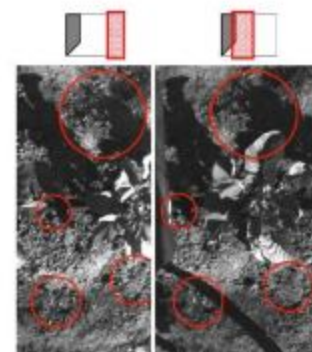

Figure 5. An example of features that can serve as markers for the stitching process. Note that both images are cropped to show only the area of the overlap, as indicated by the shaded area in the schematics above for this set taken at a 3 s interval. This area of overlap was greatly improved for the measurements with half the trigger time in 2020.

features indicated with circles. Note that the right-most image is the green channel displayed in Figure 4, cropped to the area indicated in the drawing above. As mentioned previously, the small overlapping area limited the availability of suitable marker points, which for some measurements was compensated by clear shadow patterns as seen in the topmost circle in Figure 5. On the left, a bigger rock next to the irrigation line provides a clear example of blurriness, making it more difficult to pinpoint exact coordinates to line up. At the bottom of the images, the shadow cast by the mounting structure obstructs some of the possible features, where the two rocks marked in this example could not have been identified in the wheel shadow. Finally, the circle on the lower right highlights two twigs that on the one hand demonstrate a clear change in contrast, and on the other hand indicate the distortion effects that are more profound towards the edges of the image, i.e. the twigs in the left image are distorted. Another example of the distortion becomes clear from the set of uncropped images shown in Figure 6. The irregular polygons connect the identified features in this image pair, where concentric circles mark the optical axis. On the left, the markers are on the edge of the image, at maximal distance from the optical axis, whereas on the right the same features are much closer. Note that the outer circle is fixed at the distance towards the brown marker in the latter image. For each image pair a minimum of six points were marked, with the majority being identified manually. The end result of a single measurement session is included in Figure 7a.

In 2020, with the 1.5 s interval, all images overlapped not only with the two adjacent images, but with four images, i.e. the two subsequent images in both directions. This greatly facilitated the automatic feature extraction, thereby eliminating the need for manual identification altogether. This took between 3 and 6 min, depending on the number of images, and resolution (spectral vs RGB). The pandemic impacted the maintenance and planning of the field trials substantially, which is why the development of the crops is delayed, as seen when comparing Figures 7a and b.
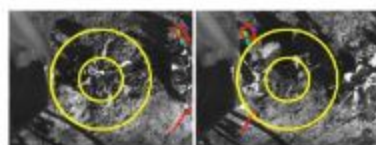

Figure 6. Coinciding markers in a green spectral image indicate clear distortion with respect to the optical axis, indicated by the concentric circles. The identified features are indicated with coloured rectangles, which are connected into irregular polygons (red) for clarity, to highlight the relative distortion.
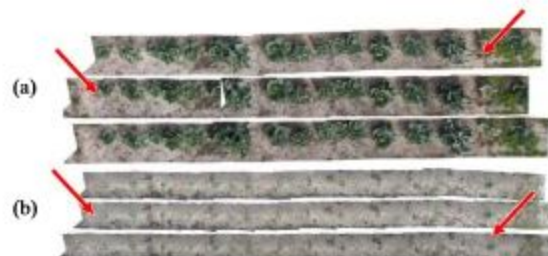

Figure 7. (a) The stitched images of November 12th 2019, taken at 3 s intervals. (b) The stitched images of November 12th 2020, taken at 1.5 s intervals. The 10 m markers are highlighted with arrows.

Discussion

The detected amount of distortion present in the images varied by 3%, which is assumed to stem from the coarseness of the reference objective in combination with the detection being assessed manually. Finer reference lines with higher contrast in each of the spectral bands might improve the accuracy of this result.

The stitching methodology presented in this work can be executed using only freely available software and does not require the use of more complex algorithms. For a proximal sensing platform with the camera mounted in a fixed nadir position and the crops aligned in the centre of the image series, the procedure can greatly be simplified, as demonstrated here. A minimal overlap of 20% appeared to be sufficient, but larger overlaps are preferred to allow automatic feature detection, as illustrated in the 2020 dataset. By regulating the speed of the fixed structure, the consistency of the obtained overlap could be further improved.

At the beginning of the growing season, this method proved sufficient to stitch a row of crop images together in a panorama fashion. For larger crops, however, the smaller distance between the camera and objective made the stitching nearly impossible, due to larger soil areas being obscured by protruding foliage. Increasing the imaging frequency or adjusting the stitching procedure would not solve this issue as sufficient distance is needed between the camera and the crop. As the main purpose of this work is early detection of nutrient deficiencies, the crops were small enough during image acquisition.

Conclusions

This work presents a simple procedure for stitching a series of close-range multi-spectral images as taken from a mobile proximal sensing platform using open-source software. The detected image distortion is corrected manually or automatically depending on the amount of image overlap. From the resulting images, vegetation indices can be calculated using any preferred software. By simplifying and automating this batch processing, the necessary processing time is greatly reduced, thereby facilitating more frequent measurement. Mosaics of multispectral imagery and deducted VIs allow for monitoring crop development per plant, rather than for swaths of land within a field, allowing for robotic maintenance to act on a level of precision not feasible in conventional PA.

Acknowledgements

References

Cardim Ferreira Lima, M., Krus, A., Valero, C., Barrientos, A., del Cerro, J. and Roldán-Gómez, J.J. (2020). Monitoring Plant Status and Fertilization Strategy through Multispectral Images, Sensors, 20(2), 435.

Fernández-Guisuraga, J.M., Sanz-Ablanedo, E., Suárez-Seoane, S. and Calvo, L. (2018). Using unmanned aerial vehicles in postfire vegetation survey campaigns through large and heterogeneous areas: Opportunities and challenges, Sensors (Switzerland), 18(2).

Franzini, M., Ronchetti, G., Sona, G. and Casella, V. (2019). Geometric and radiometric consistency of parrot sequoia multispectral imagery for precision agriculture applications, Applied Sciences (Switzerland), 9(24), 5314.

Jhan, J.P., Rau, J.Y., Haala, N. and Cramer, M. (2017). Investigation of parallax issues for multi-lens multispectral camera band co-registration, International Archives of the Photogrammetry, Remote Sensing and Spatial Information Sciences – ISPRS Archives, 157-163.

Jhan, J. P., Rau, J.Y. and Haala, N. (20180. Robust and adaptive band-to-band image transform of UAS miniature multi-lens multispectral camera, ISPRS Journal of Photogrammetry and Remote Sensing, 137, 47-60.

Jiang, J., Cai, W., Zheng, H., Cheng, T., Tian, Y., Zhu, Y., et al. (2019). Using digital cameras on an unmanned aerial vehicle to derive optimum color vegetation indices for leaf nitrogen concentration monitoring in winter wheat, Remote Sensing, 11(22).

Krus, A., Van Apeldoorn, D., Valero, C. and Ramirez, J.J. (2020). Acquiring plant features with optical sensing devices in an organic strip-cropping system, Agronomy, 10(2), 197.

Moriarty, C., Cowley, D. C., Wade, T. and Nichol, C.J. (2019). Deploying multispectral remote sensing for multi-temporal analysis of archaeological crop stress at Ravenshall, Fife, Scotland, Archaeological Prospection, 26(1), 33–46.